ACADEMIC PRESS

Available online at www.sciencedirect.com

SCIENCE DIRECT®

Journal of Sound and Vibration 262 (2003) 25–44

JOURNAL OF SOUND AND VIBRATION

www.elsevier.com/locate/jsvi

Dynamic time responses of a flexible spinning disk misaligned with the axis of rotation

Jin Wook Heo[a], Jintai Chung[a,*], Keeyoung Choi[b]

[a] *Department of Mechanical Engineering, Hanyang University, 1271 Sa-1-dong, Ansan, Kyunggi-do 425-791, Republic of Korea*

[b] *Department of Aerospace Engineering, Inha University, 253 Younghyun-dong, Nam-gu, Inchon 402-751, Republic of Korea*

Received 3 December 2001; accepted 17 June 2002

Abstract

Using the finite element method, this study investigates the dynamic time responses of a flexible spinning disk of which axis of rotation is misaligned with the axis of symmetry. The misalignment between the axes of symmetry and rotation is one of major vibration sources in optical disk drives such as CD-ROM, CD-R, CD-RW and DVD drives. Based upon the Kirchhoff plate theory and the von Karman strain theory, three coupled equations of motion for the misaligned disk are obtained: two of the equations are for the in-plane motion while the other is for the out-of-plane motion. After transforming these equations into two weak forms for the in-plane and out-of-plane motions, the weak forms are discretized by using newly defined annular sector finite elements. Applying the generalized-α time integration method to the discretized equations, the time responses and the displacement distributions are computed and then the effects of misalignment on the responses and the distributions are analyzed. The computation results show that the misalignment has an influence on the magnitudes of the in-plane displacements. It is also found that the misalignment results in the amplitude modulation or the beat phenomenon in the time responses of the out-of-plane displacement.

1. Introduction

Flexible spinning disks have wide application, for example, optical disks, hard disks and circular saws. Optical disk drives such as CD-ROM, CD-R, CD-RW and DVD drives generally demand higher data storage and faster data processing time. Because an optical disk is not

*Corresponding author. Tel.: +82-345-400-5240; fax: +82-345-406-5550.
E-mail address: jchung@hanyang.ac.kr (J. Chung).

0022-460X/03/$ - see front matter
doi:10.1016/S0022-460X(03)00018-X

permanently assembled to the spindle motor but removable from the turntable, it is practically impossible to avoid the misalignment between the axis of rotation and the axis of symmetry. In recently developed optical disk drives, the misalignment can be one of major vibration sources that may cause read/write errors. Therefore, it is necessary to investigate the effect of misalignment on the dynamic behaviours of a spinning disk.

Much research was carried out for the vibration of a spinning disk since Southwell et al. [1,2] studied the free vibration of a flexible spinning disk. Some studies considered various loading and boundary conditions [3–7]. Related to the topic of this paper, the effects of asymmetry on the disk vibration were investigated by some authors. For example, Parker and Mote [8] presented perturbation solutions to analytically determine the natural frequencies for nearly axisymmetric annular or circular disks. They also analyzed the free vibration of coupled, asymmetric disk–spindle systems in which both the disk and spindle are flexible [9]. Phylactopoulos and Adams [10,11] studied the transverse free and forced vibrations of a rectangularly orthotropic spinning disk. Kim et al. [12] investigated the effects of circumferentially varying model features on the natural frequencies and modes. In addition, Chang and Wickert [13] analyzed the forced vibration of a rotationally periodic structure when subjected to travelling wave excitation. Recently, using the Galerkin method, the effects of misalignment on the natural frequencies for a spinning disk were studied by Chung et al. [14]. In their study of the misaligned spinning disk, it was assumed that the in-plane displacements were in equilibrium while the out-of-plane displacement was in a dynamic state. Under this assumption, after the exact solutions for the in-plane displacements were obtained from the stress equilibrium, the exact solutions were plugged into the equation of the out-of-plane motion. Even though this method is convenient to compute the out-of-plane natural frequencies, it cannot analyze dynamic characteristics of the in-plane motion. Therefore, the study needs to be extended in order to include both the in-plane and out-of-plane motions.

In this paper, dynamic time responses of a spinning disk, of which axis of rotation is misaligned with the axis of symmetry, are analyzed by using the finite element method. Under the condition that the in-plane and out-of plane displacements are in a dynamic state, three equations of motion for the misaligned spinning disk are derived from Hamilton's principle. After transforming the equations of motion into two weak forms, these weak forms are discretized by using newly defined annular sector finite elements. The discretized equations are verified by comparing the natural frequencies computed in this paper with the results of reference [14]. Furthermore, the dynamic time responses of the misaligned spinning disk are computed by applying the generalized-α method [15] to the discretized equations. By investigating the computed dynamic responses, the effects of misalignment on the responses are analyzed.

2. Equations of motion

Consider a flexible spinning disk with misalignment ε, as shown in Fig. 1, where the axis of symmetry, C, is misaligned with the axis of rotation, O. Therefore, non-zero misalignment implies that the axis of symmetry does not coincide with the axis of rotation. The flexible spinning disk with thickness h rotates about O with angular speed Ω and angular acceleration $\dot{\Omega}$. The disk is

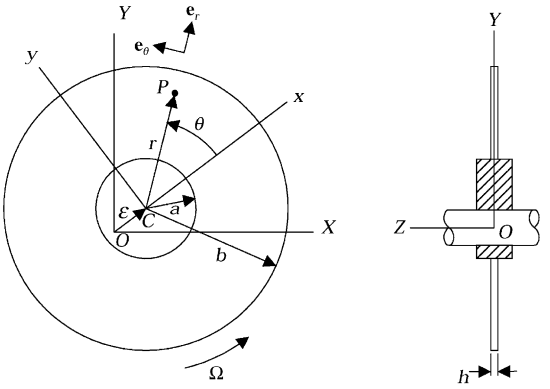

Fig. 1. Schematics of a spinning annular disk with misalignment.

clamped at the inner radius $r = a$ by a rigid clamp and is free at the outer radius $r = b$. The motion of the disk can be described by two co-ordinate systems: the XYZ and xyz co-ordinate systems. The XYZ co-ordinate system is a space-fixed co-ordinate system with the origin on the axis of rotation while the xyz co-ordinate system is a body-fixed co-ordinate system with the origin on the axis of symmetry. Hence, the unit vectors $\mathbf{e}_r$ and $\mathbf{e}_\theta$ in the xyz co-ordinate system rotate along with the disk and the co-ordinates r and θ are measured in the xyz co-ordinate system. In this paper, the equations of motions and all the associated motions are described in the body-fixed xyz coordinate system.

From the Kirchhoff plate theory, the displacements of the flexible spinning disk at time t may be written as

$$u_r(r,\theta,z,t) = u(r,\theta,t) - z\frac{\partial w(r,\theta,t)}{\partial r}, \quad u_\theta(r,\theta,z,t) = v(r,\theta,t) - z\frac{\partial w(r,\theta,t)}{r\partial\theta},$$
$$u_z(r,\theta,z,t) = w(r,\theta,t), \tag{1}$$

where u_r, u_θ and u_z are the displacements of a point in the disk in the r, θ and z directions, respectively, and u, v and w are the displacements of a point on the neutral surface of the disk in each direction. It should be noted that u, v and w are functions of t, r and θ since the disk is not axisymmetric due to misalignment ε.

The strain energy of the flexible disk is obtained from

$$U = \frac{1}{2}\int_A \varepsilon^{\mathrm{T}}\sigma \,\mathrm{d}A, \tag{2}$$

where ε is the strain vector, σ is the stress vector, and A is the area of the disk. In order to consider the coupling effect between the in-plane displacements of u and v and the out-of-plane displacement of w, the von Karman displacement–strain relations [16] are used. In this case, the strain vector may be represented by

$$\varepsilon = \begin{Bmatrix} \varepsilon_p^L + \varepsilon_p^N \\ \varepsilon_b^L \end{Bmatrix}, \tag{3}$$

where ε_p^L and ε_p^N are the linear and non-linear strain components, respectively, due to the in-plane stress while ε_b^L is the linear curvature changes due to the bending stress:

$$\varepsilon_p^L = \left\{ \frac{\partial u}{\partial r},\ \frac{\partial v}{r\partial\theta} + \frac{u}{r},\ \frac{\partial u}{r\partial\theta} + \frac{\partial v}{\partial r} - \frac{v}{r} \right\}^{\mathrm{T}}, \quad \varepsilon_p^N = \left\{ \frac{1}{2}\left(\frac{\partial w}{\partial r}\right)^2,\ \frac{1}{2}\left(\frac{\partial w}{r\partial\theta}\right)^2,\ \frac{\partial w}{\partial r}\frac{\partial w}{r\partial\theta} \right\}^{\mathrm{T}},$$

$$\varepsilon_b^L = \left\{ -\frac{\partial^2 w}{\partial r^2}, -\left(\frac{\partial w}{r\partial r} + \frac{\partial^2 w}{r^2\partial\theta^2}\right), -2\left(\frac{\partial^2 w}{r\partial r\partial\theta} - \frac{\partial w}{r^2\partial\theta}\right) \right\}^{\mathrm{T}}. \tag{4}$$

In Eqs. (3) and (4), the subscripts p and b denote the in-plane and bending contributions, respectively, whereas the superscripts L and N represent the linear and non-linear strains.

The stress–strain relation for homogeneous, isotropic, elastic and Hookean material is used in this study. Since the thickness h is much smaller than other dimensions, the stress state of the disk is under the plane-stress condition. In this case, the stress–strain relation can be written as

$$\sigma = \mathbf{D}\varepsilon, \tag{5}$$

where

$$\sigma = \begin{Bmatrix} \sigma_p \\ \sigma_b \end{Bmatrix}, \quad \mathbf{D} = \begin{bmatrix} \mathbf{D}_p & \mathbf{0} \\ \mathbf{0} & \mathbf{D}_b \end{bmatrix}. \tag{6}$$

In Eq. (6), σ_p and σ_b represent the linearized internal force vector and the internal moment vector, respectively; $\mathbf{D}_p$ and $\mathbf{D}_b$ are the elasticity matrices for the extensible rigidity and flexural rigidity:

$$\sigma_p = \{q_r, q_\theta, q_{r\theta}\}^{\mathrm{T}}, \quad \sigma_b = \{m_r, m_\theta, m_{r\theta}\}^{\mathrm{T}}, \tag{7}$$

$$\mathbf{D}_p = D_0 \begin{bmatrix} 1 & \nu & 0 \\ \nu & 1 & 0 \\ 0 & 0 & (1-\nu)/2 \end{bmatrix}, \quad \mathbf{D}_b = D \begin{bmatrix} 1 & \nu & 0 \\ \nu & 1 & 0 \\ 0 & 0 & (1-\nu)/2 \end{bmatrix}, \tag{8}$$

where

$$D_0 = \frac{Eh}{1-\nu^2}, \quad D = \frac{Eh^3}{12(1-\nu^2)}. \tag{9}$$

In the above equations, E and ν are Young's modulus and the Poisson ratio, q_r, q_θ and $q_{r\theta}$ are the linearized internal forces per unit length of the neutral surface, and m_r, m_θ and $m_{r\theta}$ are the internal moments per unit length of the neutral surface. The linearized internal forces and the moments may be expressed in terms of the displacements u, v and w:

$$q_r = D_0\left[\frac{\partial u}{\partial r} + \nu\left(\frac{u}{r} + \frac{\partial v}{r\partial\theta}\right)\right], \quad q_\theta = D_0\left[\nu\frac{\partial u}{\partial r} + \left(\frac{u}{r} + \frac{\partial v}{r\partial\theta}\right)\right], \quad q_{r\theta} = \frac{1-\nu}{2}D_0\left[\frac{\partial v}{\partial r} + \frac{\partial u}{r\partial\theta} - \frac{v}{r}\right], \tag{10}$$

$$m_r = -D\left[\frac{\partial^2 w}{\partial r^2} + \nu\left(\frac{\partial w}{r\partial r} + \frac{\partial w}{r^2\partial\theta}\right)\right], \quad m_\theta = -D\left[\nu\frac{\partial^2 w}{\partial r^2} + \frac{\partial w}{r\partial r} + \frac{\partial w}{r^2\partial\theta}\right],$$

$$m_{r\theta} = -(1-\nu)D\left(\frac{\partial^2 w}{r\partial r\partial\theta} - \frac{\partial w}{r^2\partial\theta}\right). \tag{11}$$

The kinetic energy can be expressed in terms of the velocity vector of a point in the disk. The velocity vector is obtained by differentiating the displacement vector

$$\mathbf{r} = \left(r + u - z\frac{\partial w}{\partial r} + \varepsilon\cos\theta\right)\mathbf{e}_r + \left(v - z\frac{\partial w}{r\partial\theta} - \varepsilon\sin\theta\right)\mathbf{e}_\theta + w\mathbf{e}_z, \tag{12}$$

with respect to time. Then the velocity vector may be written as

$$\mathbf{v} = \mathbf{v}_p - z\mathbf{v}_b, \tag{13}$$

where $\mathbf{v}_p$ and $\mathbf{v}_b$ are the in-plane and bending contributions, respectively:

$$\mathbf{v}_p = \left(\frac{\partial u}{\partial t} - \Omega v + \varepsilon\Omega\sin\theta\right)\mathbf{e}_r + \left[\frac{\partial v}{\partial t} + \Omega(r+u) + \varepsilon\Omega\cos\theta\right]\mathbf{e}_\theta + \frac{\partial w}{\partial t}\mathbf{e}_z, \tag{14}$$

$$\mathbf{v}_b = \left(\frac{\partial^2 w}{\partial t\partial r} - \Omega\frac{\partial w}{r\partial\theta}\right)\mathbf{e}_r + \left(\frac{\partial^2 w}{r\partial t\partial\theta} + \Omega\frac{\partial w}{\partial r}\right)\mathbf{e}_\theta. \tag{15}$$

Since the thickness h is very small, the rotary inertia effect is negligible. Therefore, the kinetic energy T is approximated to

$$T = \frac{1}{2}\rho h\int_A \mathbf{v}_p\cdot\mathbf{v}_p\,\mathrm{d}A, \tag{16}$$

where ρ is the mass density of the disk. The non-conservative virtual work δW_{nc} done by the external pressure P_w in the z direction can be written as

$$\delta W_{nc} = \int_A P_w\delta w\,\mathrm{d}A \tag{17}$$

The equations of motion and the boundary conditions are derived from Hamilton's principle

$$\delta\int_{t_1}^{t_2}(T - U + W_{nc})\,\mathrm{d}t = 0, \tag{18}$$

where t_1 and t_2 are arbitrary time. Introducing Eqs. (2), (16) and (17) into Eq. (18), the equations of motion are obtained as

$$\rho h\left(\frac{\partial^2 u}{\partial t^2} - 2\Omega\frac{\partial v}{\partial t} - \Omega^2 u - \dot{\Omega}v\right) - \frac{\partial q_r}{\partial r} - \frac{\partial q_{r\theta}}{r\partial\theta} - \frac{q_r - q_\theta}{r} = \rho h\Omega^2(r + \varepsilon\cos\theta) - \rho h\varepsilon\,\dot{\Omega}\sin\theta, \tag{19}$$

$$\rho h\left(\frac{\partial^2 v}{\partial t^2} + 2\Omega\frac{\partial u}{\partial t} - \Omega^2 v + \dot{\Omega}u\right) - \frac{\partial q_\theta}{r\partial\theta} - \frac{\partial q_{r\theta}}{\partial r} - 2\frac{q_{r\theta}}{r} = -\rho h\varepsilon\Omega^2\sin\theta - \rho h\dot{\Omega}(r + \varepsilon\cos\theta), \tag{20}$$

$$\rho h\frac{\partial^2 w}{\partial t^2} + D\nabla^4 w - \frac{\partial}{r\partial r}\left[r\left(q_r\frac{\partial w}{\partial r} + q_{r\theta}\frac{\partial w}{r\partial\theta}\right)\right] - \frac{\partial}{r\partial\theta}\left(q_{r\theta}\frac{\partial w}{\partial r} + q_\theta\frac{\partial w}{r\partial\theta}\right) = P_z, \tag{21}$$

where

$$\nabla^2 = \frac{\partial^2}{\partial r^2} + \frac{\partial}{r\partial r} + \frac{\partial^2}{r^2\partial\theta^2}. \tag{22}$$

The associated boundary conditions are given by

$$u = v = w = \frac{\partial w}{\partial r} = 0 \quad \text{at } r = a, \tag{23}$$

$$q_r = q_{r\theta} = m_r = -D\frac{\partial \nabla^2 w}{\partial r} + \frac{\partial m_{r\theta}}{r\partial \theta} = 0 \quad \text{at } r = b. \tag{24}$$

Note that Eqs. (19) and (20) for the in-plane displacements are linear equations, where only the in-plane displacements u and v are coupled with each other. On the other hand, Eq. (21) for the out-of-plane displacement is a non-linear equation. The out-of-displacement w is coupled with the in-plane displacements u and v because q_r, q_θ and $q_{r\theta}$ are functions of u and v. Therefore, it is expected that misalignment ε affects the in-plane displacements u and v as well as the out-of-plane displacement w.

3. Finite element formulation

Using the finite element method, numerical solutions are obtained from the partial differential Eqs. (19)–(21) and the boundary conditions of Eqs. (23) and (24). After the weak forms or the variational forms are derived, the spatial discretization of the weak forms leads to the initial value problem that consists of the ordinary differential equations and the corresponding initial conditions. Before deriving the weak forms, it is necessary to define the trial and weighting functions. For the two-dimensional domain A of the disk, a function φ in the Hilbert space H^1 should satisfy the following conditions: (1) φ is continuous on A, (2) $\partial\varphi/\partial r$ and $\partial\varphi/\partial\theta$ are piecewise continuous, and (3) $\int_A(\partial\varphi/\partial r)^2\,\mathrm{d}A$ and $\int_A(\partial\varphi/r\partial\theta)^2\,\mathrm{d}A$ are less than the infinity. The trial function is defined as a function in the Hilbert space H^1, satisfying all the boundary conditions, namely, both the essential and natural boundary conditions. On the other hand, the weighting function is defined as an arbitrary function in the H^1 space, which should be zero on the boundaries where the essential boundary conditions are prescribed. In this study, the trial functions for the displacements in the r, θ and z directions are denoted by u, v and w, respectively. The corresponding weighting functions are represented by $\bar{u}$, $\bar{v}$ and $\bar{w}$.

The weak forms are derived from the strong forms given by the partial differential equations and the corresponding boundary conditions. Since Eqs. (19) and (20) are coupled equations between only u and v but Eq. (21) is a coupled equation between u, v and w, two weak forms are derived in this study: one is for the in-plane motion and the other is for the out-of-plane motion. The weak form for the in-plane motion is obtained by multiplying Eqs. (19) and (20) by the weighting functions $\bar{u}$ and $\bar{v}$, respectively, summing the equations, and then integrating the resultant equation by parts over the disk area A with the divergence theorem. The weak form for the in-plane motion can be expressed as

$$\rho h\int_A \bar{\mathbf{u}}_p^{\mathrm{T}}\frac{\partial^2 \mathbf{u}_p}{\partial t^2}\,\mathrm{d}A + 2\Omega\rho h\int_A \bar{\mathbf{u}}_p^{\mathrm{T}}\mathbf{S}\frac{\partial \mathbf{u}_p}{\partial t}\,\mathrm{d}A - \Omega^2\rho h\int_A \bar{\mathbf{u}}_p^{\mathrm{T}}\mathbf{u}_p\,\mathrm{d}A + \dot{\Omega}\rho h\int_A \bar{\mathbf{u}}_p^{\mathrm{T}}\mathbf{S}\mathbf{u}_p\,\mathrm{d}A$$
$$+\int_A (\bar{\boldsymbol{\varepsilon}}_p^L)^{\mathrm{T}}\mathbf{D}_p\bar{\boldsymbol{\varepsilon}}_p^L\,\mathrm{d}A = \int_A \bar{\mathbf{u}}_p^{\mathrm{T}}\mathbf{f}_p\,\mathrm{d}A, \tag{25}$$

where

$$\mathbf{u}_p = \begin{Bmatrix} u \\ v \end{Bmatrix}, \quad \bar{\mathbf{u}}_p = \begin{Bmatrix} \bar{u} \\ \bar{v} \end{Bmatrix}, \quad \mathbf{S} = \begin{bmatrix} 0 & -1 \\ 1 & 0 \end{bmatrix}, \quad \mathbf{f}_p = \begin{Bmatrix} \rho h\Omega^2(r + \varepsilon\cos\theta) - \rho h\varepsilon\dot{\Omega}\sin\theta \\ -\rho h\varepsilon\Omega^2\sin\theta - \rho h\dot{\Omega}(r + \varepsilon\cos\theta) \end{Bmatrix}. \tag{26}$$

Similarly, the weak form for the out-of-plane motion is derived by multiplying Eq. (21) by the weighting function $\bar{w}$ and then integrating the equation by parts:

$$\rho h \int_A \bar{w}\frac{\partial^2 w}{\partial t^2}\,\mathrm{d}A + \int_A (\bar{\boldsymbol{\varepsilon}}_b^L)^{\mathrm{T}}\mathbf{D}_b\boldsymbol{\varepsilon}_b^L\,\mathrm{d}A + \int_A \bar{\boldsymbol{\theta}}^{\mathrm{T}}\mathbf{Q}\boldsymbol{\theta}\,\mathrm{d}A = \int_A \bar{w}P_z\,\mathrm{d}A, \tag{27}$$

where

$$\boldsymbol{\theta} = \begin{Bmatrix} \dfrac{\partial w}{\partial r} \\ \dfrac{\partial w}{r\partial\theta} \end{Bmatrix}, \quad \bar{\boldsymbol{\theta}} = \begin{Bmatrix} \dfrac{\partial \bar{w}}{\partial r} \\ \dfrac{\partial \bar{w}}{r\partial\theta} \end{Bmatrix}, \quad \mathbf{Q} = \begin{bmatrix} q_r & q_{r\theta} \\ q_{r\theta} & q_\theta \end{bmatrix}. \tag{28}$$

Next, consider the finite element discretization of the weak forms given by Eqs. (25) and (27). As shown in Fig. 2, by using newly defined annular sector elements, the flexible spinning disk is discretized. The annular sector element is a polar co-ordinate version of the four-node rectangular element. Hence, if transforming the polar co-ordinates to the rectangular co-ordinates, the annular sector element is mapped onto the rectangular element. The annular sector element is more efficient than the three-node triangular element and the four-node quadrilateral element, because the element has no geometric discretization error at the curved boundaries. Denoting the polar co-ordinates of the element centre by r_c and θ_c, the co-ordinates of a point on the element can be expressed as

$$r = r_c + \frac{\Delta r}{2}\xi, \quad \theta = \theta_c + \frac{\Delta\theta}{2}\eta, \quad \text{for } 0 \leqslant \xi \leqslant 1, \quad 0 \leqslant \eta \leqslant 1, \tag{29}$$

where ξ and η are co-ordinates in the parametric space, and Δr and $\Delta\theta$ define the element size.

The in-plane and out-of-plane displacements at an arbitrary point in element e can be approximated by polynomials with respect to r and θ. In this paper, the in-plane and out-of-plane displacements in the four-node annular sector element are approximated by the linear Lagrange

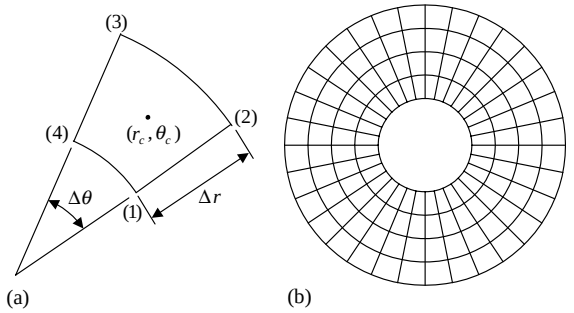

Fig. 2. Finite element model: (a) the annular sector element; and (b) construction of a finite element model.

and cubic Hermit polynomials, respectively. Therefore, polynomial approximations of u, v and w are given by

$$u = a_1 + a_2 r + a_3 \theta + a_4 r\theta, \quad v = b_1 + b_2 r + b_3 \theta + b_4 r\theta, \tag{30}$$

$$\begin{aligned} w = {} & c_1 + c_2 r + c_3 \theta + c_4 r\theta + c_5 r^2 + c_6 \theta^2 + c_7 r^2\theta + c_8 r\theta^2 + c_9 r^2\theta^2 \\ & + c_{10} r^3 + c_{11}\theta^3 + c_{12} r^3\theta + c_{13} r\theta^3 + c_{14} r^3\theta^2 + c_{15} r^2\theta^3 + c_{16} r^3\theta^3. \end{aligned} \tag{31}$$

In Eqs. (30) and (31), the coefficients, a_i, b_i and c_i can be determined from information given at the four nodes of the annular sector element. The coefficients a_i and b_i are expressed in terms of the nodal displacements u_j and v_j for $j = 1, 2, 3, 4$. On the other hand, the coefficients c_i can be also expressed in terms of the nodal values w_j, $(\partial w/\partial r)_j$, $(\partial w/\partial \theta)_j$ and $(\partial^2 w/\partial r \partial \theta)_j$. Note that the four-node annular sector element is the conforming element because the element satisfies the C^1-continuity and zero twist conditions for the out-of-plane displacement [17].

The trial functions for the in-plane and out-of-plane displacements may be expressed by

$$\mathbf{u}_p = \mathbf{N}_p^{\mathrm{T}} \mathbf{d}_p^e, \quad w = \mathbf{N}_b^{\mathrm{T}} \mathbf{d}_b^e, \tag{32}$$

where $\mathbf{N}_p$ and $\mathbf{N}_b$ are the shape function matrices for the in-plane and out-of-plane displacements, respectively; $\mathbf{d}_p^e$ and $\mathbf{d}_b^e$ are the in-plane and out-of-plane element displacement vectors given by

$$\begin{aligned} \mathbf{d}_p^e &= \{u_1, v_1, \cdots, u_4, v_4\}^{\mathrm{T}}, \\ \mathbf{d}_b^e &= \{w_1, (\partial w/\partial r)_1, (\partial w/\partial \theta)_1, (\partial^2 w/\partial r \partial \theta)_1, \ldots, w_4, (\partial w/\partial r)_4, (\partial w/\partial \theta)_4, (\partial^2 w/\partial r \partial \theta)_4\}^{\mathrm{T}}. \end{aligned} \tag{33}$$

The shape function matrices $\mathbf{N}_p$ and $\mathbf{N}_b$ are the 8×2 and 16×1 matrices, which are functions of r and θ. Similarly, the associated weighting functions are given by

$$\bar{\mathbf{u}}_p = \mathbf{N}_p^{\mathrm{T}} \bar{\mathbf{d}}_p^e, \quad \bar{w} = \mathbf{N}_b^{\mathrm{T}} \bar{\mathbf{d}}_b^e, \tag{34}$$

where $\bar{\mathbf{d}}_p^e$ and $\bar{\mathbf{d}}_b^e$ are arbitrary vectors:

$$\begin{aligned} \bar{\mathbf{d}}_p^e &= \{\bar{u}_1, \bar{v}_1, \ldots, \bar{u}_4, \bar{v}_4\}^{\mathrm{T}}, \\ \bar{\mathbf{d}}_b^e &= \{\bar{w}_1, (\partial \bar{w}/\partial r)_1, (\partial \bar{w}/\partial \theta)_1, (\partial^2 \bar{w}/\partial r \partial \theta)_1, \ldots, \bar{w}_4, (\partial \bar{w}/\partial r)_4, (\partial \bar{w}/\partial \theta)_4, (\partial^2 \bar{w}/\partial r \partial \theta)_4\}^{\mathrm{T}}. \end{aligned} \tag{35}$$

The strains and slopes in an element can also be expressed in terms of the nodal information. Substituting the displacements of Eqs. (32) into the linear strains of Eqs. (4), the linear strains can be rewritten as

$$\varepsilon_p^L = \mathbf{B}_p \mathbf{d}_p^e, \quad \varepsilon_b^L = \mathbf{B}_b \mathbf{d}_b^e, \tag{36}$$

where $\mathbf{B}_p$ and $\mathbf{B}_b$ are the 3×8 and 3×16 matrices, which are functions of r and θ. Similarly, introducing the second equation of Eq. (32) to the first equation of Eq. (28), the θ matrix may be expressed as

$$\theta = \mathbf{N}_\theta^{\mathrm{T}} \mathbf{d}_b^e, \tag{37}$$

where $\mathbf{N}_\theta$ is the 2×16 matrix function of r and θ. Meanwhile, the weighting functions for ε_p^L, ε_b^L and θ are given by

$$\bar{\varepsilon}_p^L = \mathbf{B}_p \bar{\mathbf{d}}_p^e, \quad \bar{\varepsilon}_b^L = \mathbf{B}_b \bar{\mathbf{d}}_b^e, \quad \bar{\theta} = \mathbf{N}_\theta^{\mathrm{T}} \bar{\mathbf{d}}_b^e, \tag{38}$$

The weak forms of Eqs. (25) and (27) are discretized by using the four-node annular sector elements defined in the above. After discretizing the domain A into N_e elements, i.e., the subdomains A_e, $e = 1, 2, \ldots, N_e$, as shown in Fig. 2b, introduction of Eqs. (32), (34) and (36)–(38) to Eqs. (25) and (27) yields descretized equations. The discretized equation for the in-plane motion is

$$\sum_{e=1}^{N_e} (\bar{\mathbf{d}}_p^e)^{\mathrm{T}} [\mathbf{m}_p^e \ddot{\mathbf{d}}_p^e + 2\Omega \mathbf{g}_p^e \dot{\mathbf{d}}_p^e + (\mathbf{k}_p^e - \Omega^2 \mathbf{m}_p^e + \dot{\Omega} \mathbf{g}_p^e) \mathbf{d}_p^e] = \sum_{e=1}^{N_e} (\bar{\mathbf{d}}_p^e)^{\mathrm{T}} \mathbf{f}_p^e, \tag{39}$$

where $\mathbf{m}_p^e$, $\mathbf{g}_p^e$ and $\mathbf{k}_p^e$ are the element mass, the element gyroscopic and the element stiffness matrices for the in-plane motion; $\mathbf{f}_p^e$ is the elment load vector for the in-plane motion. These element matrices and vector are given by

$$\mathbf{m}_p^e = \rho h \int_{A_e} \mathbf{N}_p \mathbf{N}_p^{\mathrm{T}} \, \mathrm{d}A, \quad \mathbf{g}_p^e = \rho h \int_{A_e} \mathbf{N}_p \mathbf{S} \mathbf{N}_p^{\mathrm{T}} \, \mathrm{d}A, \quad \mathbf{k}_p^e = \int_{A_e} \mathbf{B}_p^{\mathrm{T}} \mathbf{D}_p \mathbf{B}_p \, \mathrm{d}A, \quad \mathbf{f}_p^e = \int_{A_e} \mathbf{N}_p \mathbf{f}_p \, \mathrm{d}A. \tag{40}$$

In a similar way, the discretized equation for the out-of-plane motion is derived as

$$\sum_{e=1}^{N_e} (\bar{\mathbf{d}}_b^e)^{\mathrm{T}} [\mathbf{m}_b^e \ddot{\mathbf{d}}_b^e + (\mathbf{k}_b^e + \mathbf{k}_\theta^e) \mathbf{d}_b^e] = \sum_{e=1}^{N_e} (\bar{\mathbf{d}}_b^e)^{\mathrm{T}} \mathbf{f}_b^e, \tag{41}$$

where $\mathbf{m}_b^e$, $\mathbf{k}_b^e$ and $\mathbf{k}_\theta^e$ are the element mass, the element stiffness and the element rotation-induced stiffness matrices for the out-of-plane motion and $\mathbf{f}_b^e$ is the element load vector for the out-of-plane motion:

$$\mathbf{m}_b^e = \rho h \int_{A_e} \mathbf{N}_b \mathbf{N}_b^{\mathrm{T}} \, \mathrm{d}A, \quad \mathbf{k}_b^e = \int_{A_e} \mathbf{B}_b^{\mathrm{T}} \mathbf{D}_b \mathbf{B}_b \, \mathrm{d}A, \quad \mathbf{k}_\theta^e = \int_{A_e} \mathbf{N}_\theta \mathbf{Q} \mathbf{N}_\theta^{\mathrm{T}} \, \mathrm{d}A, \quad \mathbf{f}_b^e = \int_{A_e} P_z \mathbf{N}_b \, \mathrm{d}A. \tag{42}$$

It should be noted that $\mathbf{k}_\theta^e$ results from the membrane stresses due to rotation and it is a function of the in-plane displacement vectors $\mathbf{d}_p^e$.

The global matrix–vector equations are obtained by assembling the element matrices and vectors. Since $\bar{\mathbf{d}}_p^e$ and $\bar{\mathbf{d}}_b^e$ are arbitrary vectors, Eqs. (39) and (41) can be transformed to the global matrix–vector equations. By assembling the element matrices and vectors, the global equation for the in-plane motion is obtained as

$$\mathbf{M}_p \ddot{\mathbf{d}}_p + 2\Omega \mathbf{G}_p \dot{\mathbf{d}}_p + (\mathbf{K}_p - \Omega^2 \mathbf{M}_p + \dot{\Omega} \mathbf{G}_p) \mathbf{d}_p = \mathbf{f}_p, \tag{43}$$

where $\mathbf{d}_p$ is the global in-plane displacement vector, $\mathbf{M}_p$, $\mathbf{G}_p$ and $\mathbf{K}_p$ are the global mass, global gyroscopic and global stiffness matrices for the in-plane motion, respectively, and $\mathbf{f}_p$ is the global in-plane load vector. On the other hand, the global equation for the out-of-plane motion is written as

$$\mathbf{M}_b \ddot{\mathbf{d}}_b + [\mathbf{K}_b + \mathbf{K}_\theta(\mathbf{d}_p)] \mathbf{d}_b = \mathbf{f}_b, \tag{44}$$

where $\mathbf{d}_b$ is the global out-of-plane displacement vector; $\mathbf{M}_b$, $\mathbf{K}_b$ and $\mathbf{K}_\theta$ are the global mass, global stiffness and global rotation-induced stiffness matrices for the out-of-plane motion; $\mathbf{f}_b$ is the global out-of-plane load vector. Since the matrix $\mathbf{K}_\theta$ is a function of the in-plane displacement vector $\mathbf{d}_p$, Eq. (44) is a non-linear equation, strictly speaking. However, after $\mathbf{d}_p$ is determined from Eq. (43), Eq. (44) can be treated as a linear equation for the out-of-plane dispacement vector $\mathbf{d}_b$.

4. Verification of the finite element model

The finite element model for the spinning disk with misalignment is verified by the natural frequencies computed by the proposed method. Neglecting all the transient terms from Eq. (43), the in-plane equilibrium position vector $\mathbf{d}_p^*$ can be determined from

$$(\mathbf{K}_p - \Omega^2\mathbf{M}_p)\mathbf{d}_p^* = \mathbf{f}_p. \tag{45}$$

Since the in-plane equation of motion linearized around the equilibrium position $\mathbf{d}_p^*$ is obtained as

$$\mathbf{M}_p\ddot{\mathbf{d}}_p + 2\Omega\mathbf{G}_p\dot{\mathbf{d}}_p + (\mathbf{K}_p - \Omega^2\mathbf{M}_p)\mathbf{d}_p = \mathbf{0}, \tag{46}$$

the in-plane natural frequencies can be computed from

$$(\mathbf{K}_p - \Omega^2\mathbf{M}_p + 2\mathrm{i}\Omega\mathbf{G}_p - \omega_p^2\mathbf{M}_p)\mathbf{X}_p = \mathbf{0}, \tag{47}$$

where $\mathrm{i} = \sqrt{-1}$, ω_p is the in-plane natural frequency and $\mathbf{X}_p$ is the corresponding mode vector. On the other hand, since the out-of-plane equilibrium position vector $\mathbf{d}_b^*$ is equal to zero, the linearized version of Eq. (44) in the neighbourhood of the equilibrium position is written as

$$\mathbf{M}_b\ddot{\mathbf{d}}_b + [\mathbf{K}_b + \mathbf{K}_\theta(\mathbf{d}_p^*)]\mathbf{d}_b = \mathbf{0}, \tag{48}$$

where $\mathbf{K}_\theta(\mathbf{d}_p^*)$ is the tangent matrix of $\mathbf{K}_\theta(\mathbf{d}_p)$ at the equilibrium position. Similarly to the in-plane natural frequency, the out-of-plane natural frequency ω_b and the associated mode vector $\mathbf{X}_b$ are computed from

$$[\mathbf{K}_b + \mathbf{K}_\theta(\mathbf{d}_p^*) - \omega_b^2\mathbf{M}_b]\mathbf{X}_b = \mathbf{0}. \tag{49}$$

In order to verify the proposed finite element model, the convergence of the natural frequencies for the in-plane and out-of-plane motions is not only examined but the computed natural frequencies are also compared to those of the previous studies. For computation in this study, the material properties and dimensions are given by $b = 0.065\,\mathrm{m}$, $h = 0.0012\,\mathrm{m}$, $\rho = 1200\,\mathrm{kg/m^3}$, $v = 0.3$ and $E = 65.5 \times 10^6\,\mathrm{N/m^2}$. First, consider the convergence of the natural frequencies for the stationary disk with $a/b = 0.5$ when the disk has no misalignment. The convergence of the in-plane natural frequencies is presented in Table 1, where M and N represent the numbers of elements in the radial and tangential directions, respectively. Table 1 shows that the in-plane natural frequencies converge as M and N increase. The natural frequencies computed with $M = 10$ and $N = 32$ have very small differences from the natural frequencies computed by Srinivasan and Ramamurti [18]. The differences are 0.098%, 0.190%, 0.749% and 1.792% for the first, second, third and fourth modes, respectively. Similarly, as shown in Table 2, the out-of-plane natural frequencies of the stationary disk converge to the exact solutions provided by Mote [19]. Mode (m, n) of Table 2 stands for a mode that has m nodal circles and n nodal diameters.

Another convergence test are performed for the natural frequencies of the disk with $a/b = 3/13$ when the disk has non-zero spinning speed and misalignment. The convergence characteristics of the in-plane and out-of-plane natural frequencies when $\Omega = 1000\,\mathrm{rad/s}$ and $\varepsilon/b = 0.2$ are presented in Tables 3 and 4. These tables demonstrate that the in-plane and out-of-plane natural frequencies converge with the number of elements. Comparison of the computed in-plane natural frequencies with other solutions is not included in Table 3, because there is no pervious study on the in-plane natural frequencies for the misaligned spinning disk. Table 4 shows that the converged out-of-plane natural frequencies are slightly different from the results of Ref. [14]. In

Table 1
Convergence characteristics of the natural frequencies (rad/s) for the in-plane motion when $\Omega = \dot{\Omega} = 0$, $a/b = 0.5$ and $\varepsilon = 0$

Mode	M	N			
		8	16	24	32
First	4	4425.2771	4425.2771	4425.2771	4425.2771
	6	4410.3228	4410.3228	4410.3228	4410.3228
	8	4405.0983	4405.0983	4405.0983	4405.0983
	10	4402.6816	4402.6816	4402.6816	4402.6816
	Ref. [18]			4398.3687	
Second	4	5937.9237	5871.6487	5859.7305	5855.5857
	6	5921.5516	5855.0190	5843.0578	5838.8982
	8	5915.7647	5849.1416	5837.1652	5833.0004
	10	5913.0752	5846.4102	5834.4268	5830.2596
	Ref. [18]			5819.9220	
Third	4	9501.6901	8763.8408	8640.8246	8598.8397
	6	9472.1547	8730.4692	8607.1146	8565.0345
	8	9461.5451	8718.4879	8595.0130	8552.8992
	10	9456.5829	8712.8854	8589.3545	8547.2251
	Ref. [18]			8483.6721	
Fourth	4	12095.5368	11383.1151	10985.9642	10855.6500
	6	12021.6871	11296.0851	10896.6447	10765.8360
	8	11992.9633	11265.1609	10864.8535	10733.8494
	10	11979.6419	11250.7575	10850.0374	10718.9388
	Ref. [18]			10530.2776	

Table 4, the subscripts s and a represent the symmetric and asymmetric modes generated due to misalignment. These differences are caused by the fact that the in-plane displacements in Ref. [14] are computed from static equilibrium conditions. This means that the in-plane displacements are determined by neglecting the in-plane inertia terms. When the in-plane inertia terms are neglected, that is, when the in-plane displacements are determined from $\mathbf{K}_p\mathbf{d}_p^* = \mathbf{f}_p$ instead of Eq. (45), the out-of-plane natural frequencies converge to those of Ref. [14], as shown in Table 5. Consequently, it may be concluded that the natural frequencies of Table 4 are more accurate than those of Table 5.

5. Dynamic time responses

Dynamic time responses of the misaligned spinning disk are computed numerically by applying the generalized-α time integration method [15] to Eqs. (43) and (44). Since the matrix–vector equation for the in-plane motion, given by Eq. (43), is not coupled with the out-of-plane displacement, the time responses for the in-plane displacements can be obtained from only Eq. (43). The generalized-α method for Eq. (43) can be expressed as

$$\mathbf{M}_p\mathbf{a}^p_{n+1-\alpha_m} + 2\Omega\mathbf{G}_p\mathbf{v}^p_{n+1-\alpha_f} + (\mathbf{K}_p - \Omega^2\mathbf{M}_p + \dot{\Omega}\mathbf{G}_p)\mathbf{d}^p_{n+1-\alpha_f} = \mathbf{f}^p_{n+1-\alpha_f}, \tag{50}$$

Table 2
Convergence characteristics of the natural frequencies (rad/s) for the out-of-plane motion when $\Omega = \dot{\Omega} = 0$, $a/b = 0.5$ and $\varepsilon = 0$

Mode	M	N			
		8	16	24	32
(0,0)	4	261.5639	261.5639	261.5639	261.5639
	6	261.5391	261.5391	261.5391	261.5391
	8	261.5348	261.5348	261.5348	261.5348
	10	261.5336	261.5336	261.5336	261.5336
	Ref. [19]			261.5329	
(0,1)	4	266.9062	266.9056	266.9055	266.9055
	6	266.8737	266.8731	266.8731	266.8731
	8	266.8680	266.8674	266.8674	266.8674
	10	266.8664	266.8658	266.8658	266.8658
	Ref. [19]			266.8646	
(0,2)	4	295.4806	295.3449	295.3375	295.3362
	6	295.4205	295.2848	295.2773	295.2760
	8	295.4094	295.2737	295.2662	295.2650
	10	295.4063	295.2706	295.2631	295.2619
	Ref. [19]			295.2590	
(0,3)	4	375.5433	373.0540	372.9067	372.8814
	6	375.4382	372.9483	372.8009	372.7756
	8	375.4177	372.9277	372.7803	372.7550
	10	375.4118	372.9217	372.7743	372.7491
	Ref. [19]			372.7320	

where

$$\mathbf{d}^p_{n+1-\alpha_f} = (1-\alpha_f)\mathbf{d}^p_{n+1} + \alpha_f \mathbf{d}^p_n, \quad \mathbf{v}^p_{n+1-\alpha_f} = (1-\alpha_f)\mathbf{v}^p_{n+1} + \alpha_f \mathbf{v}^p_n,$$
$$\mathbf{a}^p_{n+1-\alpha_m} = (1-\alpha_m)\mathbf{a}^p_{n+1} + \alpha_m \mathbf{a}^p_n, \quad \mathbf{f}^p_{n+1-\alpha_f} = \mathbf{f}_p((1-\alpha_f)t_{n+1} + \alpha_f t_n),$$
$$\mathbf{d}^p_{n+1} = \mathbf{d}^p_n + \Delta t \mathbf{v}^p_n + (1/2-\beta)\Delta t^2 \mathbf{a}^p_n + \beta \Delta t^2 \mathbf{a}^p_{n+1}, \quad \mathbf{v}^p_{n+1} = \mathbf{v}^p_n + (1-\gamma)\Delta t \mathbf{a}^p_n + \gamma \Delta t \mathbf{a}^p_{n+1}, \tag{51}$$

in which α_m, α_f, β and γ are the algorithmic parameters; Δt is the time step size, i.e., $\Delta t = t_{n+1} - t_n$; $\mathbf{d}^p_n$, $\mathbf{v}^p_n$ and $\mathbf{a}^p_n$ are approximations to $\mathbf{d}_p$, $\dot{\mathbf{d}}_p$ and $\ddot{\mathbf{d}}_p$, respectively. On the other hand, application of the generalized-α method to the out-of-plane equation of motion, given by Eq. (44), leads to

$$\mathbf{M}_b \mathbf{a}^b_{n+1-\alpha_m} + [\mathbf{K}_p + \mathbf{K}_\theta(\mathbf{d}^p_{n+1-\alpha_f})]\mathbf{d}^b_{n+1-\alpha_f} = \mathbf{f}^b_{n+1-\alpha_f}, \tag{52}$$

where

$$\mathbf{d}^b_{n+1-\alpha_f} = (1-\alpha_f)\mathbf{d}^b_{n+1} + \alpha_f \mathbf{d}^b_n, \quad \mathbf{v}^b_{n+1-\alpha_f} = (1-\alpha_f)\mathbf{v}^b_{n+1} + \alpha_f \mathbf{v}^b_n,$$
$$\mathbf{a}^b_{n+1-\alpha_m} = (1-\alpha_m)\mathbf{a}^b_{n+1} + \alpha_m \mathbf{a}^b_n, \quad \mathbf{f}^b_{n+1-\alpha_f} = \mathbf{f}_b((1-\alpha_f)t_{n+1} + \alpha_f t_n),$$
$$\mathbf{d}^b_{n+1} = \mathbf{d}^b_n + \Delta t \mathbf{v}^b_n + (1/2-\beta)\Delta t^2 \mathbf{a}^b_n + \beta \Delta t^2 \mathbf{a}^b_{n+1}, \quad \mathbf{v}^b_{n+1} = \mathbf{v}^b_n + (1-\gamma)\Delta t \mathbf{a}^b_n + \gamma \Delta t \mathbf{a}^b_{n+1}, \tag{53}$$

Table 3
Convergence characteristics of the in-plane natural frequencies (rad/s) for the disk when $\Omega = 1000\,\text{rad/s}$, $\dot{\Omega} = 0\,\text{rad/s}^2$, $a/b = 3/13$ and $\varepsilon/b = 0.2$

	Mode				
M	N	First	Second	Third	Fourth
4	8	1193.0261	3020.0777	4483.0893	6540.7180
	16	1193.0261	2895.9096	4358.9330	5462.8217
	24	1193.0261	2873.8387	4336.5290	5283.9194
	32	1193.0261	2866.1816	4328.7324	5222.9675
6	8	1177.2158	2991.2514	4471.6461	6500.1545
	16	1177.2158	2865.5652	4346.3377	5409.7905
	24	1177.2158	2843.2284	4323.7273	5228.5180
	32	1177.2158	2835.4795	4315.8590	5166.7382
8	8	1171.0595	2980.2714	4467.0432	6485.1987
	16	1171.0595	2853.9982	4341.2825	5390.0581
	24	1171.0595	2831.5584	4318.5911	5207.8622
	32	1171.0595	2823.7738	4310.6947	5145.7586
10	8	1168.0609	2974.9626	4464.7564	6478.0357
	16	1168.0609	2848.4046	4338.7742	5380.5614
	24	1168.0609	2825.9149	4316.0432	5197.9116
	32	1168.0609	2818.1130	4308.1330	5135.6488

in which $\mathbf{d}_n^b$, $\mathbf{v}_n^b$ and $\mathbf{a}_n^b$ are approximations to $\mathbf{d}_b$, $\dot{\mathbf{d}}_b$ and $\ddot{\mathbf{d}}_b$, respectively. Note that Eq. (52) is a non-linear equation because the out-of-plane displacement vector $\mathbf{d}_{n+1-\alpha_f}^b$ is multiplied by the in-plane displacement vector $\mathbf{d}_{n+1-\alpha_f}^p$. However, at each time step, once the in-plane displacement vector is determined by Eqs. (50) and (51), Eq. (52) becomes a linear equation for the out-of-plane displacement vector. Consequently, the use of a non-linear equation solver, e.g., the Newton–Raphson method, can be avoided, even if Eq. (52) is intrinsically non-linear.

To verify the computation method proposed in this paper, the dynamic time responses of the in-plane and out-of-plane displacements are compared with the time responses presented in Ref. [7] when the spinning disk has no misalignment, i.e., when $\varepsilon = 0$. The material properties and dimensions for computation are the same as those of the above computation except the inner radius a that is given by $a/b = 0.268$. The zero initial conditions are applied to the disk and the unit impulsive pressure is applied in the z direction. The angular spinning speed and the corresponding acceleration are defined by

$$\Omega = \begin{cases} 3000\,t & \text{for } 0 \leqslant t \leqslant 0.1, \\ 300 & \text{for } 0.1 \leqslant t \leqslant 0.3, \\ -3000\,t + 1200 & \text{for } 0.3 \leqslant t \leqslant 0.4, \end{cases} \tag{54}$$

where the units of Ω and t are rad/s and s, respectively. Under this condition, the time responses are computed by using 240 uniform annular sector elements. The time responses for the in-plane and out-of-plane displacements are plotted in Fig. 3, where the solid and dotted lines represent the

Table 4
Convergence characteristics of the out-of-plane natural frequencies (rad/s) for the disk when $\Omega = 1000$ rad/s, $\dot{\Omega} = 0$ rad/s^2, $a/b = 3/13$ and $\varepsilon/b = 0.2$

M	N	Mode						
		(0, 0)	$(0, 1)_s$	$(0, 1)_a$	$(0, 2)_s$	$(0, 2)_a$	$(0, 3)_s$	$(0, 3)_a$
4	8	791.7123	1250.741	1130.310	1524.730	1525.478	1911.851	1957.362
	16	776.7704	1259.404	1131.055	1524.962	1525.432	1928.589	1930.412
	24	773.8691	1260.953	1131.064	1524.582	1525.095	1927.012	1928.965
	32	772.8428	1261.490	1131.056	1524.396	1524.924	1926.311	1928.313
6	8	782.7980	1243.314	1124.500	1521.914	1522.727	1910.776	1953.610
	16	767.4241	1252.237	1125.397	1522.209	1522.768	1926.337	1928.210
	24	764.4232	1253.827	1125.420	1521.826	1522.430	1924.743	1926.753
	32	763.3604	1254.377	1125.415	1521.637	1522.257	1924.034	1926.096
8	8	778.7333	1240.077	1121.940	1520.260	1521.108	1909.520	1951.056
	16	763.0889	1249.111	1122.906	1520.579	1521.179	1924.456	1926.379
	24	760.0267	1250.718	1122.933	1520.192	1520.839	1922.846	1924.912
	32	758.9416	1251.274	1122.930	1520.000	1520.665	1922.130	1924.251
10	8	776.6247	1238.495	1120.657	1519.352	1520.220	1908.732	1949.542
	16	760.8172	1247.589	1121.657	1519.683	1520.309	1923.308	1925.265
	24	757.7184	1249.204	1121.686	1519.293	1519.967	1921.687	1923.791
	32	756.6199	1249.762	1121.683	1519.100	1519.792	1920.966	1923.127
Ref. [14]		767.8218	1234.090	1115.989	1511.689	1512.136	1916.746	1918.082

time responses computed by the present study and Ref. [7], respectively. In Fig. 3, the present method shows no difference in the in-plane displacements from Ref. [7] but a small difference in the out-of-plane displacement. This difference may be caused by the fact that the present method does not use a non-liner equation solver while the method of Ref. [7] does.

The effects of misalignment on the dynamic time responses of the in-plane and out-of-plane displacements are investigated based on computation results from the proposed finite element analysis. All the material properties and dimensions are the same as the previous computation except the inner radius given by $a/b = 3/13$. The spinning speed profile is given in Fig. 4, where the angular speed linearly increases from zero to 1000 rad/s during 0.1 s and then it remains at a constant speed. Similar to the previous computation, the uniform pressure of $P_z(r, \theta, t) = 0.1\delta(t)$ is applied in the z direction. The disk is discretized with 240 annular sector elements and the time step size is selected as $\Delta t = 0.0005$s.

First, consider the effects of misalignment on the dynamic time responses of the in-plane displacements. Fig. 5 shows the dynamic time responses of the radial and tangential displacements at a point corresponding to $r = b$ and $\theta = \pi/4$ when the spinning speed is prescribed by Fig. 4. Fig. 5a shows that the patterns of the in-plane responses are similar regardless of misalignment but the amplitudes of the responses are influenced by the misalignment. In the region of constant angular speed, the radial displacement u oscillates about 0.7693 and 1.3374 mm for misalignments

Table 5
Convergence characteristics of the out-of-plane natural frequencies (rad/s) for the disk with $\Omega = 1000$ rad/s, $a/b = 3/13$ and $\varepsilon/b = 0.2$ when the in-plane equilibrium position is computed by ignoring the in-plane inertia term

		Mode						
M	N	(0, 0)	$(0, 1)_s$	$(0, 1)_a$	$(0, 2)_s$	$(0, 2)_a$	$(0, 3)_s$	$(0, 3)_a$
4	8	799.1636	1235.796	1123.488	1516.763	1517.200	1910.016	1949.331
	16	786.6104	1243.391	1124.173	1517.194	1517.458	1925.709	1926.886
	24	784.1980	1244.741	1124.189	1516.928	1517.220	1924.552	1925.805
	32	783.3467	1245.208	1124.185	1516.790	1517.092	1924.027	1925.308
6	8	790.5888	1228.216	1117.648	1513.888	1514.380	1908.710	1945.658
	16	777.7293	1236.012	1118.464	1514.387	1514.720	1923.375	1924.567
	24	775.2456	1237.393	1118.491	1514.120	1514.483	1922.214	1923.484
	32	774.3681	1237.871	1118.490	1513.981	1514.354	1921.686	1922.985
8	8	786.7168	1224.936	1115.090	1512.238	1512.758	1907.388	1943.206
	16	773.6605	1232.820	1115.966	1512.765	1513.129	1921.523	1922.738
	24	771.1324	1234.214	1115.997	1512.496	1512.891	1920.354	1921.650
	32	770.2387	1234.695	1115.997	1512.355	1512.761	1919.823	1921.149
10	8	784.7208	1223.337	1113.813	1511.338	1511.874	1906.573	1941.761
	16	771.5443	1231.269	1114.719	1511.880	1512.262	1920.405	1921.637
	24	768.9894	1232.669	1114.752	1511.609	1512.023	1919.231	1920.545
	32	768.0859	1233.152	1114.753	1511.468	1511.892	1918.697	1920.042
Ref. [14]		767.8218	1234.090	1115.989	1511.689	1512.136	1916.746	1918.082

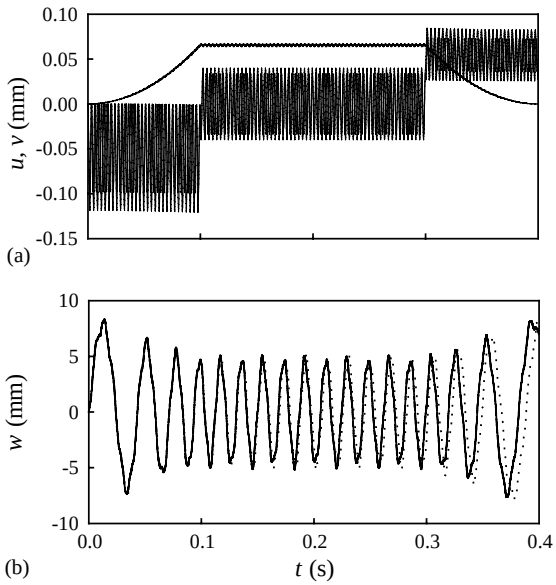

Fig. 3. Comparison of the dynamic time responses for (a) the in-plane displacements and (b) the out-of-plane displacements between the present study and Ref. [7] when $a/b = 0.268$ and $\varepsilon = 0$: ———, present study; …… Ref. [7].

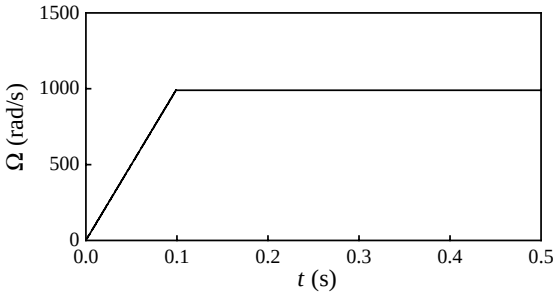

Fig. 4. Angular speed profile of the spinning disk.

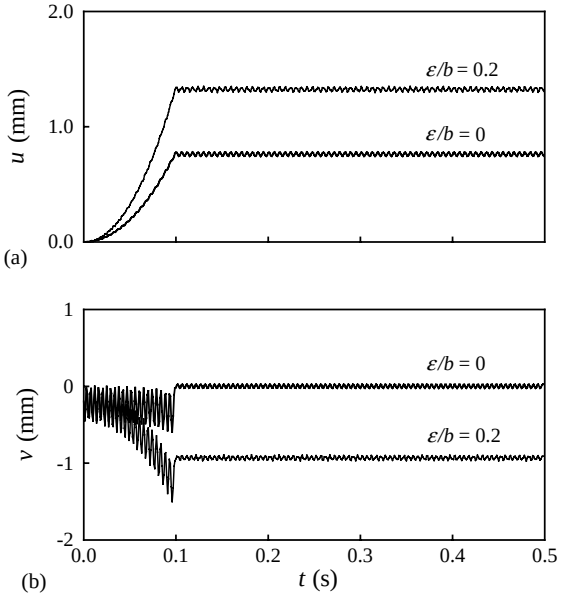

Fig. 5. Dynamic time responses of the in-plane displacements at $r = b$ and $\theta = \pi/4$ for the angular speed profile of Fig. 4 when $a/b = 3/13$: (a) the radial displacement u; and (b) the tangential displacement v.

of $\varepsilon/b = 0$ and $\varepsilon/b = 0.2$, respectively. The average value of $u = 0.7693$ mm in the constant speed region has a very small difference from the exact solution of 0.7672 mm given by Timoshenko and Goodier [20]. The tangential displacement is also affected by the misalignment. Fig. 5b illustrates that the tangential displacement of a point corresponding to $r = b$ and $\theta = \pi/4$ oscillates about zero when the disk has no misalignment. However, for the disk with misalignment $\varepsilon/b = 0.2$, the tangential displacement of the same point oscillates about $v = -0.9426$ mm.

The effect of misalignment on the in-plane displacements can also be described by a deformed shape of the disk when the misaligned spinning disk is in a steady sate. In Fig. 6, the solid line represents the deformed shape while the dashed line represents the undeformed shape. The deformed shape is amplified with a scale factor of 5. It is observed that the deformed shape is not axisymmetric but it is symmetric with respect to the x-axis, namely, the extended line connecting

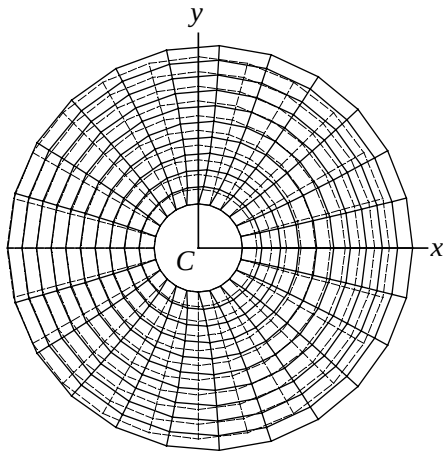

Fig. 6. Deformed shape of the disk due to the in-plane displacements when $a/b = 3/13$, $\Omega = 1000\,\text{rad/s}$, $\dot{\Omega} = 0$ and $\varepsilon/b = 0.2$. ——, deformed shape; ----------, undeformed shape.

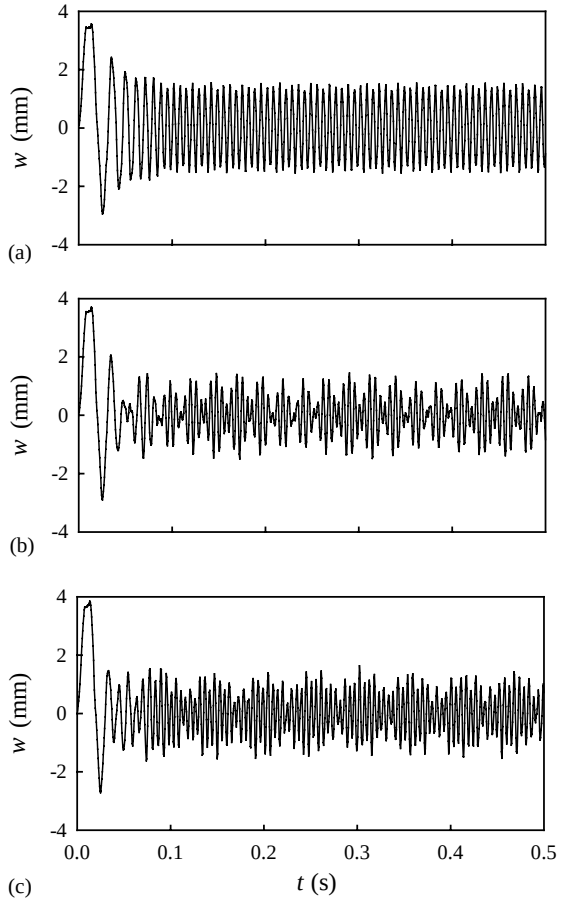

Fig. 7. Dynamic time responses of the out-of-plane displacement w at $r = b$ and $\theta = \pi/4$ for the angular speed profile of Fig. 4 when $a/b = 3/13$: (a) $\varepsilon/b = 0$; (b) $\varepsilon/b = 0.1$; and (c) $\varepsilon/b = 0.2$.

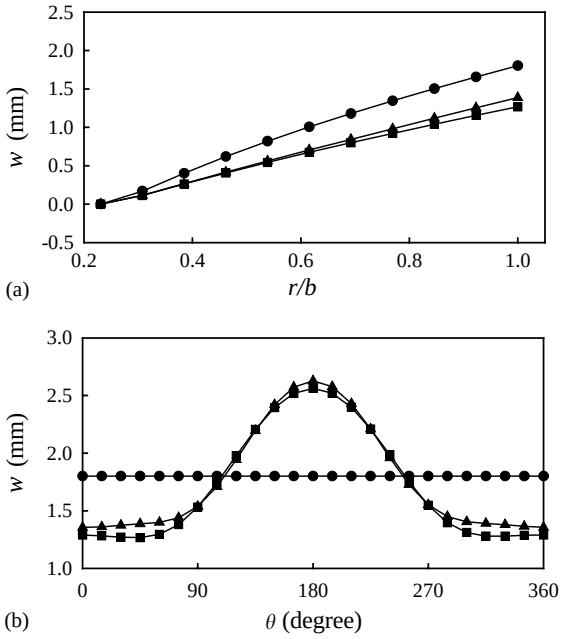

Fig. 8. Distributions for the r.m.s. values of the out-of-plane displacement w during $0.1 \leqslant t \leqslant 0.5$ when $a/b = 3/13$, $\Omega = 1000$ rad/s, and $\dot{\Omega} = 0$: (a) along the radial line at $\theta = \pi/4$; and (b) along the outer circumference at $r = b$. —●—, $\varepsilon/b = 0$; —■—, $\varepsilon/b = 0.1$; —▲—, $\varepsilon/b = 0.2$.

the centroid and the rotation centre. The radial and tangential displacements increase with the distance from the rotation centre and they have the maximum values at the outer radius. On the other hand, for the variation of the circumferential co-ordinate θ, the radial and tangential displacements change according to patterns of $\cos\theta$ and $\sin\theta$.

Next, the effects of misalignment on the out-of-plane displacement are investigated when the disk has $a/b = 3/13$ and its angular speed is prescribed by Fig. 4. The out-of-plane responses for different values of misalignment are shown in Fig. 7. The responses are computed at a point defined by $r = b$ and $\theta = \pi/4$. During the interval of positive acceleration, i.e., $0 \leqslant t \leqslant 0.1$, the stiffening effect due to the centrifugal force decreases the amplitudes and periods as the angular speed increases. When the disk has no misalignment, the vibration amplitudes do not change significantly in the region of the constant angular speed, i.e., $0.1 \leqslant t \leqslant 0.5$, as shown in Fig. 7a. However, in the case of non-zero misalignment, the out-of-plane displacement exhibits amplitude modulation. Figs. 7b and c, which corresponds to $\varepsilon/b = 0.1$ and 0.2 respectively, demonstrate the amplitude modulation. This amplitude modulation, which is often called the beat phenomenon, is observed when the natural frequencies are slightly different. As shown in Table 4, when misalignment exists, the mode $(0, n)$ for $n \neq 0$ is split into the symmetric and asymmetric modes, which have slightly different natural frequencies. A more detailed discussion on the symmetric and asymmetric modes can be found in Refs. [8,21].

The influence of misalignment on the distributions of the out-of-plane displacement is depicted in Fig. 8, where the square, the circle and the triangle correspond $\varepsilon/b = 0$, 0.1 and 0.2,

respectively. In Fig. 8, the values of the vertical axis are the root-mean-square (r.m.s.) values computed for the out-of-plane displacement during $0.1 \leqslant t \leqslant 0.5$, i.e., during the time when the angular speed is constant. The distributions in the radial direction, as shown in Fig. 8a, demonstrate that the r.m.s. values at $\theta = \pi/4$ monotonically increase with the radius and they have the maximum values at the outer radius. On the other hand, an influence of misalignment on the circumferential distributions of the out-of-plane displacement is described in Fig. 8(b), where the r.m.s. values are computed at $r = b$. The r.m.s. value of the out-of-plane displacement has a uniform distribution along the outer circumference when there exists no misalignment. However, when the misalignment is not zero, the r.m.s. value at the outer circumference changes as a function of θ. In the case of non-zero misalignment, the r.m.s. value has the maximum value at $\theta = 180^\circ$ while it has the minimum value around $\theta = 0^\circ$. Note that a point corresponding to $r = b$ and $\theta = 0^\circ$ is the farthest point from the axis of rotation and a point corresponding to $r = b$ and $\theta = 180^\circ$ is the nearest point. Therefore, the r.m.s. value increases as the distance from the axis of rotation decreases. This phenomenon results from the fact that the stiffening effect due to rotation becomes large with the distance from the axis of rotation to the outer circumference.

6. Conclusions

The dynamic time responses of a flexible spinning disk, which has misalignment between the disk axis and the rotation axis, are analyzed by using the finite element method. For analysis, the equations of motion are derived for the in-plane and out-of-plane motions. Two linear equations for the in-plane motion have coupling between only the in-plane displacements while a non-linear equation for the out-of-plane motion has coupling between the out-of-plane and in-plane displacements. Based on the equations of motion, two global matrix–vector equations are obtained by using the newly defined annular sector finite elements: one is for the in-plane motion and the other is for the out-of-plane motion. Dynamic time responses are computed by adopting the generalized-α time integration method without a non-linear equation solver.

It is shown from the time responses for the in-plane motion that, when a disk has misalignment, the amplitudes of in-plane displacements at a given angular position increase with the radius while they change with patterns of cosine or sine functions in the circumferential direction. The corresponding deformed shape due to the in-plane displacements is symmetric with respect to the extended line connecting the centroid and the rotation centre. On the other hand, it is observed that the misalignment yields the amplitude modulation or the beat phenomenon in the time responses for the out-of-plane displacement. This modulation verifies that the modes of the misaligned disk are split into the symmetric and asymmetric modes that have slightly different natural frequencies. Finally, it is found that the r.m.s. value for the out-of-plane displacement increases as the distance from the axis of rotation decreases.

Acknowledgements

The authors are grateful for the financial support provided by a grant (Grant Number R01-2000-00292) from the Korea Science and Engineering Foundation (KOSEF).

References

[1] H. Lamb, R.V. Southwell, The vibration of a spinning disk, Proceedings of the Royal Society 99 (1921) 272–280.
[2] R.V. Southwell, On the free transverse vibrations of a uniform circular disc clamped at its centre; and on the effects of rotation, Proceedings of the Royal Society 101 (1922) 133–153.
[3] W. Everseman, R.O. Dodson, Free vibration of a centrally clamped spinning circular disk, AIAA Journal 7 (1969) 2010–2012.
[4] W.D. Iwan, T.L. Moeller, The stability of a spinning elastic disk with a transverse load system, American Society of Mechanical Engineers, Journal of Applied Mechanics 43 (1976) 485–490.
[5] R.C. Benson, D.B. Bogy, Defection of a very flexible spinning disk due to a stationary transverse load, American Society of Mechanical Engineers, Journal of Applied Mechanics 45 (1978) 636–642.
[6] I.Y. Shen, Y. Song, Stability and vibration of a rotating circular plate subjected to stationary in-plane edge loads, American Society of Mechanical Engineers, Journal of Applied Mechanics 63 (1996) 121–127.
[7] J. Chung, J.-E. Oh, H.H. Yoo, Non-linear vibration of a flexible spinning disc with angular acceleration, Journal of Sound and Vibration 231 (2000) 375–391.
[8] R.G. Parker, C.D. Mote, Exact perturbation for the vibration of almost annular or circular plates, Journal of Vibration and Acoustics 118 (1996) 436–445.
[9] R.G. Parker, C.D. Mote, Vibration and coupling phenomena in asymmetric disk-spindle systems, American Society of Mechanical Engineers, Journal of Applied Mechanics 63 (1996) 953–961.
[10] A. Phylactopoulos, G.G. Adams, Transverse vibration of a rectangularly orthotropic spinning disk, Part 1: formulation and free vibration, American Society of Mechanical Engineers, Journal of Vibration and Acoustics 121 (1999) 273–279.
[11] A. Phylactopoulos, G.G. Adams, Transverse vibration of a rectangularly orthotropic spinning disk, Part 2: forced vibration and critical speeds, American Society of Mechanical Engineers, Journal of Vibration and Acoustics 121 (1999) 280–285.
[12] M. Kim, J. Moon, J.A. Wickert, Spatial modulation of repeated vibration modes in rotationally periodic structures, American Society of Mechanical Engineers, Journal of Vibration and Acoustics 122 (2000) 62–68.
[13] J.Y. Chang, J.A. Wickert, Response of modulated doublet modes to travelling wave excitation, Journal of Sound and Vibration 242 (2001) 69–83.
[14] J. Chung, J.W. Heo, C.S. Han, Natural frequencies of a spinning disk misaligned with the axis of rotation, Journal of Sound and Vibration 260 (2003) 763–775.
[15] J. Chung, G.M. Hulbert, A time integration algorithm for structural dynamics with improved numerical dissipation: the generalized-α method, American Society of Mechanical Engineers, Journal of Applied Mechanics 60 (1993) 371–375.
[16] O.C. Zienkiewicz, R.L. Taylor, The Finite Element Method, Vol. 2., MaGraw-Hill, London, 1991.
[17] J.N. Reddy, An Introduction to the Finite Element Method, MaGraw-Hill, New York, 1993.
[18] V. Srinivasan, V. Ramamurti, Dynamic response of an annular disk to a moving concentrated, in-plane edge load, Journal of Sound and Vibration 72 (1980) 251–262.
[19] C.D. Mote, Stability of circular plates subjected to moving loads, Journal of The Franklin Institute 290 (1970) 329–344.
[20] S. Timoshenko, J.N. Goodier, Theory of Elasticity, McGraw-Hill, New York, 1970.
[21] J. Chung, J.M. Lee, Vibration analysis of a nearly axisymmetric shell structure using a new finite ring element, Journal of Sound and Vibration 219 (1999) 35–50.